Ceramics International xxx (xxxx) xxx–xxx

Contents lists available at ScienceDirect

Ceramics International

journal homepage: www.elsevier.com/locate/ceramint

A novel α-Fe_2O_3@MoS_2QDs heterostructure for enhanced visible-light photocatalytic performance using ultrasonication approach

Gomaa Khabiri[a,b,*], Abdelaziz M. Aboraia[a,c,**], Malak Soliman[a], A.A. Guda[a], V.V. Butova[a,d], I.S. Yahia[e,f], A.V. Soldatov[a]

[a] Smart Materials Research Institute, Southern Federal University, Sladkova 178/24, 344090, Rostov-on-Don, Russia
[b] Physics Department, Faculty of Science, Fayoum University, Fayoum, 63514, Egypt
[c] Department of Physics, Faculty of Science, Al-Azhar University, Assiut, 71542, Egypt
[d] Federal Research Center of the Southern Scientific Center of the Russian Academy of Sciences, 344006, Rostov-on-Don, Russia
[e] Advanced Functional Materials & Optoelectronic Laboratory (AFMOL), Department of Physics, Faculty of Science, King Khalid University, P.O. Box 9004, Abha, Saudi Arabia
[f] Metallurgical Lab., Nanoscience Laboratory for Environmental and Bio-medical Applications (NLEBA), Semiconductor Lab., Physics Department, Faculty of Education, Ain Shams University, Roxy, 11757, Cairo, Egypt

ARTICLE INFO

Keywords:
Fe_2O_3@MoS_2QDs nanocomposite
Hydrothermal
Ultrasonication approach
(MB)
And photocatalytic degradation

ABSTRACT

Constructing excellent heterojunction to improve the photocatalytic performance of materials is critically important. Herein, we report an effective simple, easy preparation method for α-Fe_2O_3@MoS_2QDs nanocomposite via two two-step process, including hydrothermal and ultrasonication approaches. The as-prepared materials were characterized using X-ray diffraction (XRD), Transmission electron microscope (TEM), TGA, X-ray fluorescence (XRF) and photoluminescence spectra (PL). The refined PXRD patterns of α-Fe_2O_3 photocatalyst confirm the formation of a single trigonal phase of Fe_2O_3 without another phase impurities. When the MoS_2 QDs were coupled with α-Fe_2O_3, the phase was changed to a single monoclinic phase with C 2/C space group and no peaks observed for MoS_2 QDs. Morphological analyses reveal the successful formation of Fe_2O_3@MoS_2QDs nanocomposites with uniform distribution of MoS_2 QDs on the Fe_2O_3 surface. The XRF analysis confirmed the presence of Mo, S, and Fe elements indicating the nanocomposite formation. The Uv–vis results revealed the enhancement of absorption capability of the α-Fe_2O_3@MoS_2QDs material, particularly in the white light region. Very noticeably, the as-prepared α-Fe_2O_3@MoS_2QDs exhibit high photocatalytic activity performance (84%) toward methylene blue (MB) in 1 min under visible light irradiation. The superior photocatalytic performance of the prepared material can be attributed to the enhancement of the light absorption and the high separation efficiency of photogenerated electron-hole pair in Fe_2O_3@MoS_2QDs structure, which confirmed by PL analysis. The mechanism of photocatalytic degradation of MB over Fe_2O_3@MoS_2QDs nanocomposite was suggested. This work provides a new, low-cost and straightforward idea for enhancement of the degradation performance of organic pollutants in water.

1. Introduction

Hematite (α-Fe_2O_3) is an attractive material because of has several features, for instance, the most stable iron oxides, cheap cost, non-toxic, abundance, and the production is simple [1–5]. α-Fe_2O_3 has numerous applications in several aspects, such as in magnetic materials, water purifications, catalysts, sensors, pigments, molecular imaging, biomedical applications including drug delivery systems, and energy storage, particularly Lithium-ion batteries as a cathode material [6–10]. Besides, owing to α-Fe_2O_3 has a low bandgap of 2–2.2 eV, it is a promising visible-light material since, it absorbs the most of visible light and thus, it can utilize as a photocatalyst [11–14]. Nevertheless, it is challenging to separate the photo-induced electron-hole pairs in α-Fe_2O_3, which limits their further use as an active photocatalyst. Currently, several routes utilize to synthesize α-Fe_2O_3, for instance, sol-gel, hydrothermal, microwave-assisted solvothermal, and combustion method [15–17]. With the change of the preparation method, the shape, size, and morphology of the particles can be changed [18]. The morphology and size

* Corresponding author. Smart Materials Research Institute, Southern Federal University, Sladkova 178/24, 344090, Rostov-on-Don, Russia.
** Corresponding author. Smart Materials Research Institute, Southern Federal University, Sladkova 178/24, 344090, Rostov-on-Don, Russia.
E-mail addresses: gma01@fayoum.edu.eg (G. Khabiri), a.m.aboraia@gmail.com (A.M. Aboraia).

https://doi.org/10.1016/j.ceramint.2020.05.021
Received 12 March 2020; Received in revised form 25 April 2020; Accepted 2 May 2020

of α-Fe_2O_3 have an essential role in the performance of a photocatalyst [19]. It is worth mentioning that the pristine α-Fe_2O_3 has a low efficiency of photocatalytic in the visible range irradiation, low specific surface area, fast recombination, and short lifespan of light-generated electron-hole pairs, so many studies were carried out to improve the separation efficiency of photogenerated electron-hole pairs [12,15].

To enhance the photocatalyst activity via improving the separation of photogenerated electrons and holes, Peng et al. [20] prepared the heterostructures of Fe_2O_3/TiO_2 photocatalysts with different loading ratios of Fe^{3+} on the surface of TiO_2. They claimed that the Fe_2O_3/TiO_2 heterostructures have high an efficient degradation for Orange II compared to pure TiO_2 and Fe_2O_3 and they attributed these results to the high separation for the electron-hole pair generation in the Fe_2O_3/TiO_2 photocatalyst. In the same way, Zhu et al. [21] obtained photocatalytic activity of the α-Fe_2O_3@SnO_2 core − shell structure much higher than the pristine α-Fe_2O_3 or SnO_2 for Rhodamine B. Zhang and co-works [22] found that the coupling of RGO and α-Fe_2O_3 enhanced the photocatalytic activity of the RGO -α-Fe_2O_3 heterostructure and this can be ascribed to the good charge carrier transfer in the heterostructure and the large active sites of RGO for dye degradation.

It is clear for us that graphene has several characteristics that possess distinctive physical and chemical properties, and the molybdenum disulfide (MoS_2) has a similar layered structure [23,24]. Owing to a small bandgap 1.7 eV and high active sites, the nanoscale MoS_2 is recognized as a potential photocatalyst and adsorbent material [25–28]. The incorporation of MoS_2 in metal oxide nanoparticles can reduce the bandgap, which will effectively facilitate the transport of light-emitted electron-hole pairs. Besides, the MoS_2 and noble metals have a similar role, since the sheets of MoS_2 can serve as electron collectors, which can be used to separate electron-hole pairs. Furthermore, two-dimensional layered structure MoS2 leads to increased surface area and strong integration with oxide materials [29,30].

Compared to bulk-MoS_2 or MoS_2 nanosheets, MoS_2 quantum dots (MoS_2 QDs) have received more attention because of its high stability in aqueous media and more number of active edge atoms. MoS_2 QDs can be prepared via several methods, including liquid exfoliation [31], hydrothermal [32], and lithium intercalation [33]. However, in some preparation techniques, the preparation can involve complicated procedures and be time-consuming. Therefore, developing a fast, simple, nontoxic, and one-step solution method to synthesize MoS_2 QDs remains a challenge. The coupling of MoS_2 QDS with semiconductors and catalyst materials can enhance the photocatalytic performance. For example, Sun and co-authors [34] reported an enhancement in the photocatalytic H_2 production when CdS decorated with MoS_2 QDS, compared to CdS and Bulk MoS_2–CdS photocatalyst.

Presently, we shine a light for the first time on the enhancement of the photocatalytic performance of α-Fe_2O_3@MoS_2 QDs heterostructure fabricated by ultrasonication techniques. The structural properties of the prepared materials were studied by XRD before and after the photocatalytic experiment and there is only one phase of α-Fe_2O_3 was observed. The coating of α-Fe_2O_3 by MoS_2 QDs investigated by TEM. The optical absorption capability and the electron and hole generated pairs separation of the Fe_2O_3@MoS_2 QDs photocatalyst were significantly enhanced. In order to evaluate the possibility of treatment of polluted water in this work, the photocatalytic degradation experiments toward MB were carried out. We demonstrated that owing to the above obtained structural and optical results, the Fe_2O_3@MoS_2 QDs material exhibits superior photocatalytic efficiency.

2. Experimental section

2.1. Materials

Ammonium molybdate ($(NH_4)_2MoO_4$), Thiourea (CH_4N_2S), were used to prepare Molybdenum disulfide (MoS_2) as chemical reagents. Iron nitrate (Fe $(NO_3)_3$), starch ($C_6H_{10}O_5$) used to prepare α-Fe_2O NPs.

3. Materials preparation

3.1. Preparation of α-Fe_2O NPs

Iron oxide powder synthesis was performed by means of a solid-state combustion method: metal nitrate salt; iron nitrate used as an oxidant in the combustion reaction and starch ($C_6H_{10}O_5$) was used as a fuel for combustion. The synthetic technique is based on the reaction of oxidation 5 g of starch used as a fuel, was added to one male of Fe $(NO_3)_2$, and grinded together and placed on a hot plate in an oven at 60 °C for 24 h. The resulting samples were evaporated to dryness at 80 °C for 2 h and had very high foam content. The foam was decomposed at 600 °C for 3 h to eject carbon in the form of CO_2 resulting from the combustion of starch – nitrate mixture.

3.2. Preparation of MoS_2 nanoflowers

The MoS_2 nanoflowers were prepared via one-step through [27]. Specifically, 1.811 g of Ammonium molybdate and 0.557 g of thiourea were dissolved in 44 ml of distilled water under stirring for several minutes. The mixture was put into Teflon-lined stainless steel autoclave with filling ratio of 44% and heated at temperature 180 °C for 20 h. The mixture was then cooled suddenly. The precipitate was then collected, centrifuged, and washed several times by methanol and distilled water, then dried at 80 °C for 24 h.

3.3. Preparation of MoS_2 QDs

For preparation MoS_2 QDs, the ultrasonic mixing method was used [35]. 50 mg of the obtained black MoS_2 nanosheets were then added into 50 ml of distilled water and sonicated for 2–3 h until a good suspension was obtained. To separate the supernatant (MoS_2 QDs), the obtained suspension was centrifuged at 18,000 rpm for 80 min. The supernatant obtained was referred to as 1T-MoS_2 QDs.

3.4. Fabrication of α-Fe_2O_3@MoS_2QDs nanocomposite

Photocatalysts α-Fe_2O_3@MoS_2QDs was fabricated through ultrasonic mixing techniques. First, 50 mg of α-Fe_2O_3 was dispersed into 30 distilled water for several mints. After that, 10 ml of MoS_2 QDs (0.004 g) were added to the α-Fe_2O_3 solution and the mixture was sonicated for 1h. Then, the obtained mixture was centrifuged, washed, and dried for 24 h at 60 °C to give α-Fe_2O_3@MoS_2QDs material.

3.5. Characterization techniques

X-ray powder diffraction (XRD) measurements were conducted using X-ray diffractometer Bruker D2 Phaser and recorded with a 2θ range of 5–90 and 0.01 steps. The morphology analyses were characterized using transmission electron microscopy (Tecnai G2 Spirit Bio TWIN) operating at 120 kV. The chemical compositions of the prepared materials were determined using X-ray fluorescence spectrometer (SPARK-1-2M). Photoluminescence spectra (PL) spectra were investigated using Agilent Cary Eclipse optical fluorescence spectrophotometer. Thermogravimetry and differential scanning calorimetry were analyzed STA 449 F5 Jupiter. NANO-flex determined the particle size of the prepared materials based on the dynamic light scattering (DLS) effect. The optical properties of the prepared samples were conducted through spectrophotometer Shimadzu UV-2600. The absorbance spectra were operated in the 190–900 nm range with the air reference.

3.6. Photocatalytic experiment

The photocatalytic experiments of the prepared materials were conducted by degrading MB in an aqueous solution (10 ppm) at room temperature and under white light illumination. 10 mg catalyst dosage

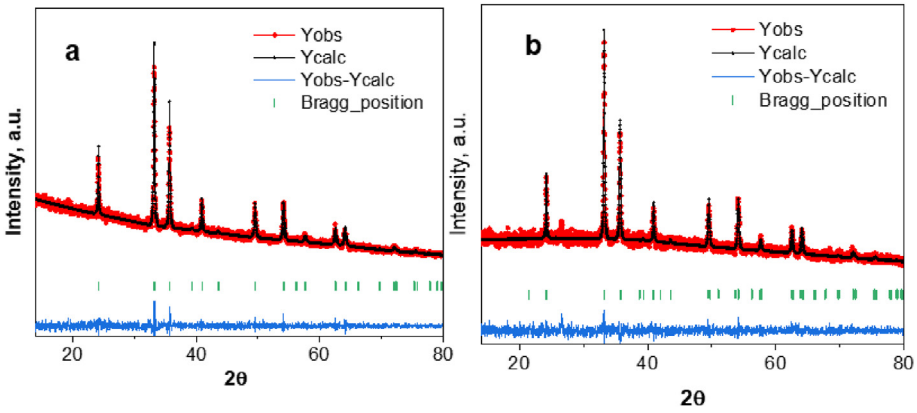

Fig. 1. The XRD pattern for (a) pristine α-Fe_2O_3 and (b) α-Fe_2O_3@MoS_2QDs materials.

wad added to the dye solution. Under dark condition, the solution was stirred to eliminate the dark adsorption. After that, the solution was then irradiated by tungsten lamp. Afterward, 5 ml of the solution was taken out at regular intervals and centrifuged at 3000 rpm for 5 min to remove the material and then analyzed via UV–Vis spectrometer.

4. Results and discussion

4.1. Crystal structure

The refined PXRD patterns of pure Fe_2O_3 and Fe_2O_3 coated by MoS_2 QDs materials are shown in Fig. 1a and b. It is clear that Fe_2O_3 exhibits a single trigonal phase without any contaminations by another phase and has a space group of R -3c according to crystallography (Cod: 9015964). The peaks of diffraction were clearly seen at 24.09^0, 33.31^0, 40.85^0, 49.4^0, 54.05^0, 57.5^0, 62.4^0, 64.24^0 and 72.11^0 and corresponding to (012), (104), (110), (113), (024), (116), (214) and (300) planes. Otherwise, Fig. 4b shows that the α-Fe_2O_3@MoS_2QDs nanocomposite has a single monoclinic phase with C 2/C space group, which is in agreement with the crystallography database (Cod: 2108027). Besides, no peaks are detected for MoS_2 QDs, which can due to the ultrasmall MoS_2 QDs size and the low amount of it MoS_2 QDs, which will be confirmed by XRF analysis.

From refinements via Fullprof program, the Lattice parameters, volume, and the space group of the prepared materials are obtained and reported in Table 1. We noted the phase changed for α-Fe_2O_3@MoS_2QDs after α-Fe_2O_3 coating by MoS_2 QDs. This change refers to the method of coating since the sonication is utilized to help to exfoliate the nanoparticles and decreased the size. Moreover, this change is an indication of the successful formation of α-Fe_2O_3@MoS_2QDs nanocomposite.

4.2. Synthesis mechanism of α-Fe_2O_3@MoS_2QDs nanocomposites

Fabrication of α-Fe_2O_3@MoS_2QDs nanocomposites were obtained through the growth of MoS_2 QDs on the α-Fe_2O_3 surface, as shown in Fig. 2. First, the MoS_2 QDs were prepared via a combination of a hydrothermal method at 180 °C and sonication treatment. MoS_2 nanosheet was obtained by adjusting the molar ration of Mo to S to 1:4 and the filling ratio of the autoclave to 45%. Then, 50 mg of MoS_2 was sonicated for several hours and centrifuged for 90 min to remove the precipitate. The obtained suspension is named MoS_2 QDs. The MoS QDs have several advantages, such as good dispersion and ultrasmall particle size, allowing them to deposit on the α-Fe_2O_3 surface. After that, 50 mg of the α-Fe_2O_3 was added to 10 mg of MoS QDs (0.004 g) and sonicated for around 1 h until wholly mixed and form α-Fe_2O_3@MoS_2QDs nanocomposites.

Table 1
Lattice parameters (a, b, and c), volume and space group of α-Fe_2O_3 and α-Fe_2O_3@MoS_2QDs samples.

Sample	a (Å)	b (Å)	c (Å)	v $(Å)^3$	Space group
α-Fe_2O_3	5.03200	5.03200	13.74207	301.345	R −3 c
Fe_2O_3@MoS_2	9.61720	5.02901	13.74149	200.994	C 1 2/c 1

4.3. Morphology analysis

To visualize the microstructure and the size of the α-Fe2O3 NPs and α-Fe_2O_3@MoS_2QDs materials, TEM measurements were performed at different ad magnifications, as shown in Fig. 3 a-d. It is noticeable that the MoS_2 QDs are uniformly distributed with no evident agglomeration (Fig. 3 a, b). For α-Fe_2O_3@MoS_2QDs sample (Fig. 3 c, d), it can be seen that the hematite α-Fe_2O_3 is in nanoscale, however, the nanoparticles are seemed agglomerated and exhibit large particles size. Moreover, the TEM images of α-Fe_2O_3@MoS_2QDs nanocomposites, illustrate that the MoS_2 QDs are successfully attached into the α-Fe_2O_3 surface, which is helpful for the charge carrier transferee in the heterostructures and thus could increase the photocatalytic efficiency of the α-Fe_2O_3@MoS_2QDs. Fig. 3 e, f demonstrates the particle size distribution of the MoS_2 QDS and α-Fe_2O_3@MoS_2QDs samples. Obviously, the MoS_2 QDs exhibit homogenous ultrasmall size distribution in the range of 2–7 nm with an average diameter of 4.5 nm. Also, the α-Fe_2O_3@MoS_2QDs material has an average particle size of 149.5 nm.

4.4. X-ray fluorescence

The chemical composition of the α-Fe_2O_3@MoS_2QDs samples was investigated using XRF analysis. Table .2 displays the chemical compositions of the prepared material. It is noteworthy that the main constituents of the α-Fe_2O_3@MoS_2QDs material are Fe, Mo, and S with an atomic mass ratio of 95.07%: 1.08%: 1.59%., respectively. In addition, some residues of calcium, chlorine, and titanium as chemical impurities with very low percentages are present. These results demonstrate that the MoS_2 QDs are successfully attached to the surface of α-Fe_2O_3. The obtained percent mass ratios of Fe: Mo: S obtained by XRF is consistent with the amounts used initially to prepare the α-Fe_2O_3@MoS_2QDs composites.

4.5. Uv–vis analysis

In order to study the influence of MoS_2 QDs on the optical properties of the α-Fe_2O_3 NPs, the Uv–vis spectrum was investigated for the pure α-Fe2O3 NPs and α-Fe_2O_3@MoS_2QDs nanocomposites. Fig. 4 a. shows the ultraviolet–vis absorption spectrum of pristine α-Fe2O3 NPs and α-Fe_2O_3@MoS_2QDs composites, respectively. The absorption spectrum of

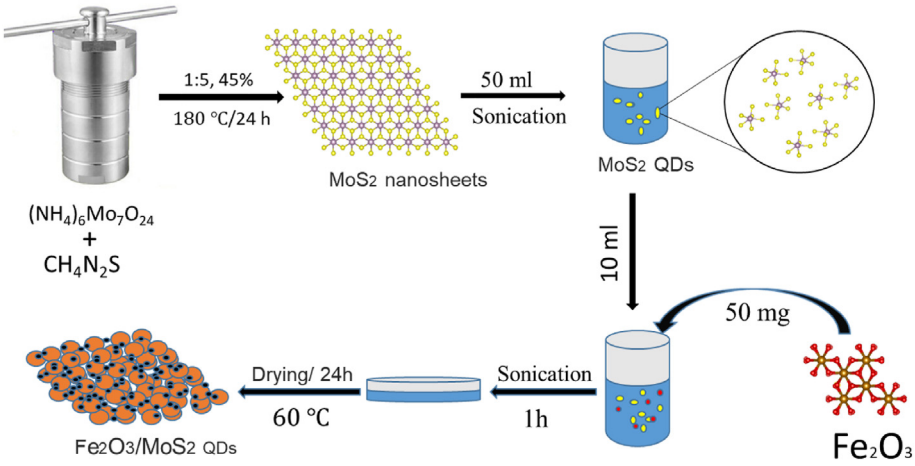

Fig. 2. Schematic description of the fabrication route the α-Fe_2O_3@MoS_2QDs nanocomposites.

pristine α-Fe_2O_3 was in UV region. However, the spectrum of α-Fe_2O_3@MoS_2QDs exhibits high absorption in the Ultraviolet and visible region, implying the MoS_2-QDs enhances the absorption spectrum, particularly in the visible light region of 400–600 nm. The enhancement of light absorption may be attributed to the loading of MoS_2 QDs on the surface of pristine α-Fe_2O_3. This is consistent with the change of color of samples, as shown in the insert image in Fig. 4.b. The bandgap (E_g) of the prepared materials was calculated using Tauc's equation [36] (Fig. 4 b). The α-Fe_2O_3@MoS_2QDs shows a bandgap of about 2.22 eV, which is lower than pure α-Fe_2O_3 (2.54 eV). The bandgap results show that the combination of α-Fe_2O_3 with MoS_2 QDs causes the narrowing of the bandgap of the α-Fe_2O_3, indicating that MoS_2 QDs plays a significant role in the prepared composites. The improvement of the absorption ability of the α-Fe_2O_3@MoS_2QDs nanocomposites in the visible light could increase the photo-electron holes pairs generation that participates in the reaction, which is desirable for the photocatalytic process [37].

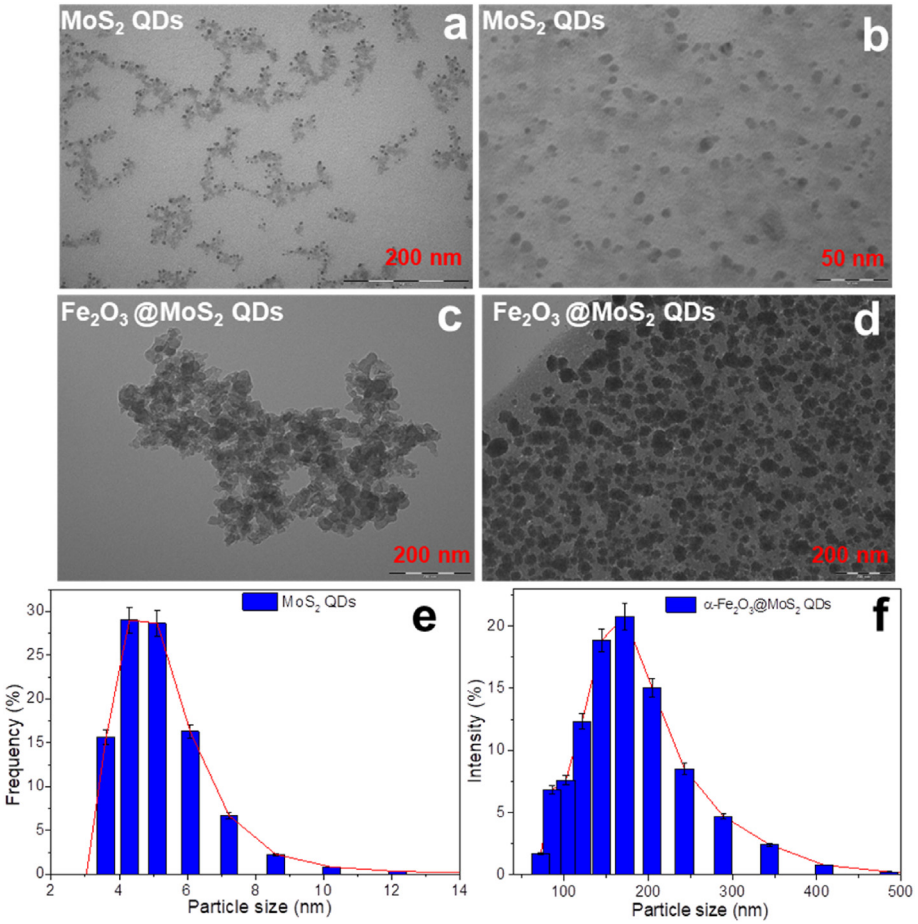

Fig. 3. TEM images of (a, b) MoS_2 QDs-, (c, d) α-Fe_2O_3@MoS_2 QDs sample, and (e, f) the corresponding particle size.

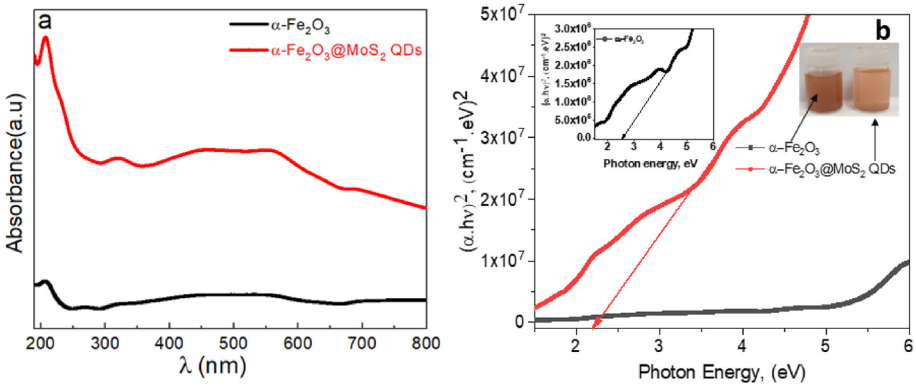

Fig. 4. (a) Uv–vis spectra and (b) Tauc plots of pure α-Fe2O3 NPs and α-Fe_2O_3@MoS_2QDs nanocomposites. Inset: color change of samples. (For interpretation of the references to color in this figure legend, the reader is referred to the Web version of this article.)

Table 2
Chemical composition of α-Fe_2O_3@MoS_2QDs material using XRF analysis.

Element	Percentage (100%)
Fe	95.07
Mo	1.08
S	1.59
Cl	0.87
Ca	0.61
Ti	0.66

4.6. PL analysis

Photoluminescence (PL) analysis is commonly applied to investigate carrier migration, trapping, and transition. The emission PL comes from the recombination of photogenerated electron-hole pair; thus it can be used to explain the effectiveness of the charge carries and as well as determined the charge carrier lifetime in the heterostructures [38,39]. The peak intensity indicates the transfer capability of the photogenerated electrons and holes [40]. The higher PL intensity reflects the higher recombination rate of the electron-hole pairs, and therefore, the lowers photocatalytic performance. Fig. 5 displays the PL spectra of the studied materials. It can be seen that the PL intensity of the α-Fe_2O_3 is much higher than that of α-Fe_2O_3@MoS_2QDs nanocomposites suggesting the high lifetime of the electron-hole pair of the α-Fe_2O_3@MoS_2QDs nanocomposites. Combined with the morphology examination of the Fe_2O_3@MoS_2QDs nanocomposites, the heterojunctions formed between α-Fe_2O_3 and MoS_2QDs leads to an improvement in the electron-hole pair separation [41], in which the MoS_2 QDs, can act as a good electron acceptor during the photocatalytic process and therefore, the migration of the electrons is increased. In light of the above analysis, the obtained results demonstrate that the long electron-hole lifetime and the high light absorption can enhance the photocatalytic activity of the Fe_2O_3@MoS_2QDs nanocomposites, which confirms the photocatalytic results. The bandgap of the prepared materials was calculated from the PL spectroscopy (Fig.SI2). For α-Fe_2O_3@MoS_2QDs the bandgap was found be smaller than pure α-Fe_2O_3, which consistent with Uv–vis results.

4.7. BET specific surface area

To investigate the porous properties and the surface area of the prepared samples a nitrogen adsorption–desorption isotherm is studied (Fig. 6). It is clear that the materials have typical IV isotherms with hysteresis loop, indicating the existing of the mesoporous structure. The BET surface area of the α-Fe_2O_3@MoS_2QDs (5.8518 m^2/g) samples was found to be slightly larger than α-Fe_2O_3 (5.3898 m^2/g). The slightly enhancement of the surface area can be ascribed to the emerging micropores formed at the interface between the MoS_2 QDs and α-Fe_2O_3 material.

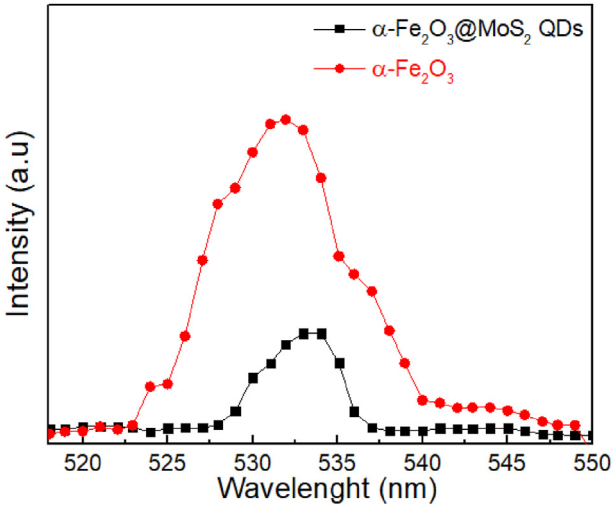

Fig. 5. PL spectra of α-Fe_2O_3 and α-Fe_2O_3@MoS_2QDs nanocomposites.

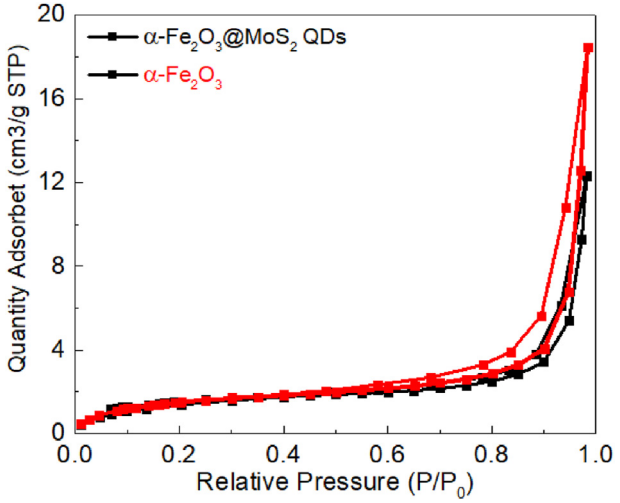

Fig. 6. Nitrogen adsorption-desorption isotherm curve of α-Fe_2O_3 and α-Fe_2O_3@MoS_2QDs

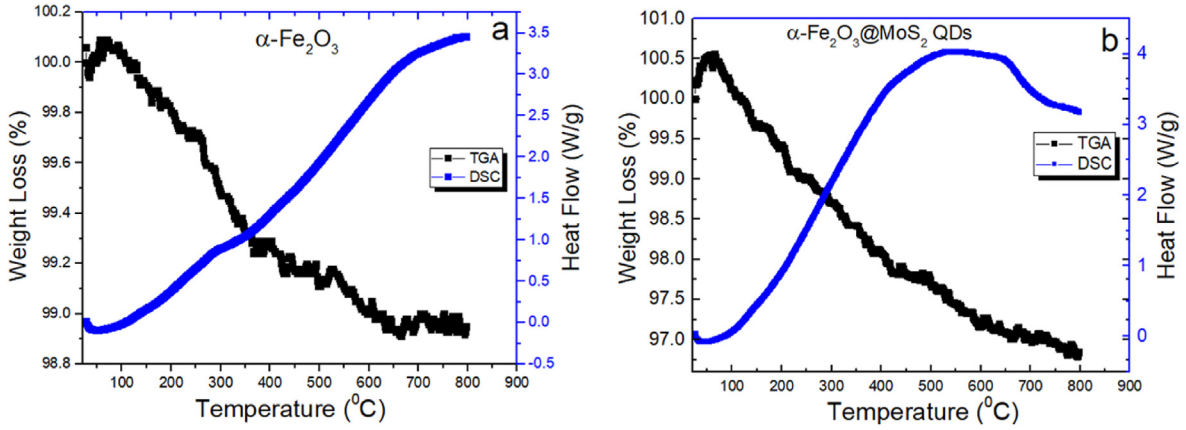

Fig. 7. TGA and DSC of the α-Fe_2O_3 and α-Fe_2O_3@MoS_2QDs samples.

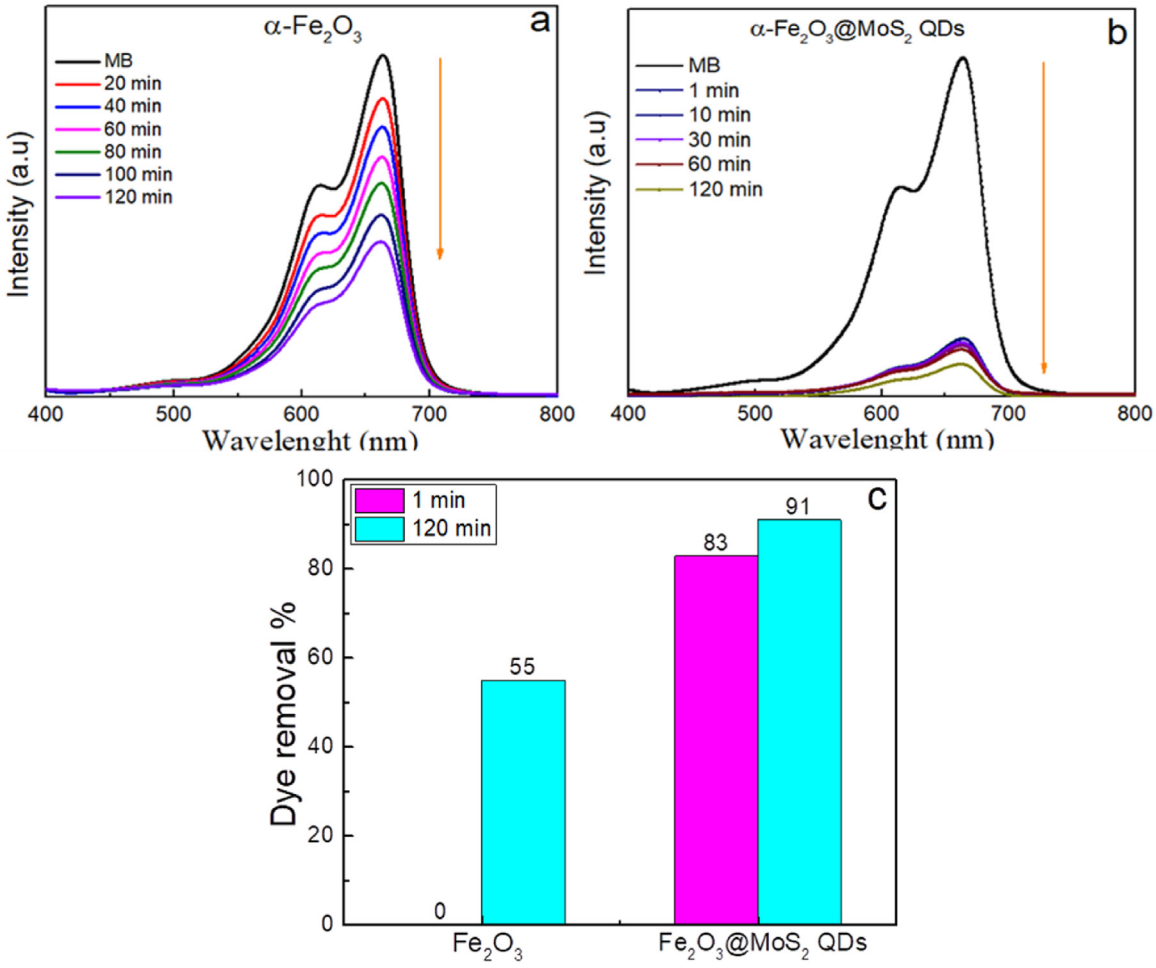

Fig. 8. UV-via spectra of the photocatalytic activity of MB for (a) α-Fe_2O_3, (b) α-Fe_2O_3@MoS_2QDs, and (c) plot of efficiency values.

4.8. Thermogravimetric analysis (TGA) and differential scanning calorimetry (DSC)

In order to study the thermal stability of the studied materials, the TGA and DSC analysis of the α-Fe2O3 NPs and α-Fe_2O_3@MoS_2QDs samples have been simultaneously conducted in the temperature range up to 800 °C (Fig. 7). From DSC analysis, the peak observed at 100 °C for both samples could be ascribed to dehydration phenomena [42]. Moreover, the observed exothermic peak in the range of 350–700 for α-Fe_2O_3@MoS_2QDs samples, reflect the influence of MoS_2 QDs. As shown in TG analysis, the total weight loss in the α-Fe2O3 NPs and α-Fe_2O_3@MoS_2QDs samples is 1.06 wt % and 3.04 wt %, respectively. The losses at 100 °C for both samples are corresponding to the small endothermic peak on the DSC curve. Also, there is no notably mass loss above 650 °C for α-Fe_2O_3 and 750 °C for α-Fe_2O_3@MoS_2QDs, revealing that under air atmosphere the appropriate cancelation temperature is 650 and 750 for α-Fe_2O_3 and α-Fe_2O_3@MoS_2QDs, respectively.

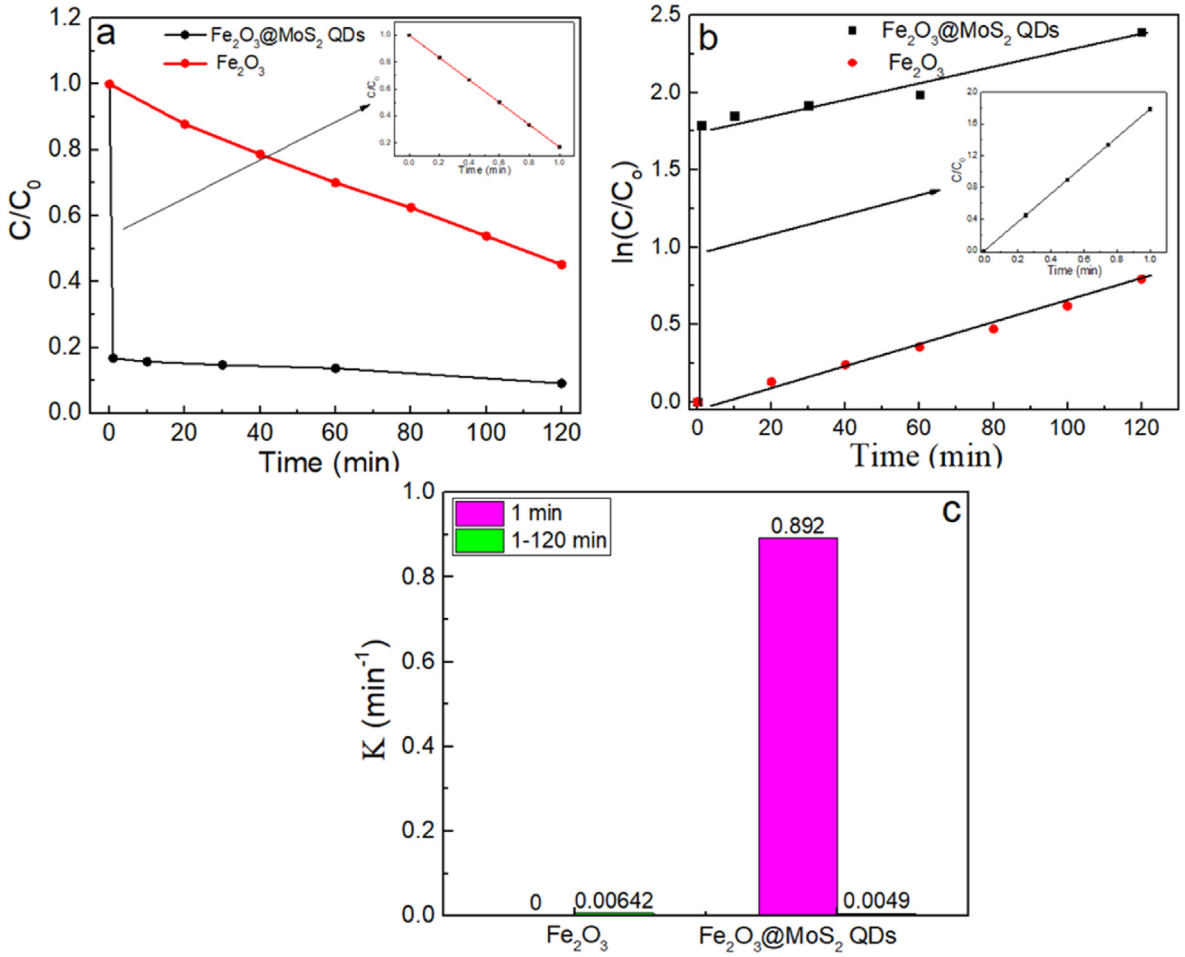

Fig. 9. (a) Degradation efficiency (C/C_0) of the prepared samples, (b) Second-order kinetics of MB photocatalytic degradation, and (d) Rate constant plots (K min^{-1}) for α-Fe_2O_3 and α-Fe_2O_3@MoS_2QDs.

Table 3
Comparison of photocatalytic activity of Fe_2O_3 based materials.

Catalyst	Dyes	Reaction time	Degradation rate (%)	Reference
α-Fe2O3/MoS2	RhB	75 min	98	[15]
RGO-Fe_2O_3–MoS_2	MB	50 min	99	[45]
GO-Fe_2O_3–TiO_2	MB	150 min	98	[47]
Fe_2O_3-RGO	MB	180 min	100	[22]
Fe_2O_3-RGO	RhB	150 min	92	[48]
MoS_2-RGO-Fe_2O_3	MB	80 min	36	[49]
αFe_2O_3@MoS_2QDs	MB	1 min	84	Present work

4.9. Photocatalytic studies

The photocatalytic activity performance of pure α-Fe_2O_3 and α-Fe_2O_3@MoS_2QDs nanocomposites was investigated by quantifying the degradation of MB aqueous solution under visible light irradiation at room temperature as shown in Fig. 8a–c. It is clear that the pure α-Fe_2O_3 (Fig. 7a) showing relatively low photocatalytic efficiency with a degradation rate of 55% within 120 min. The low photocatalytic activity of the pure α-Fe_2O_3 towards different dyes such as MB and MO and RhB was reported previously [43–46] and can attribute to the insufficient photogenerated charge separation and low transferability.

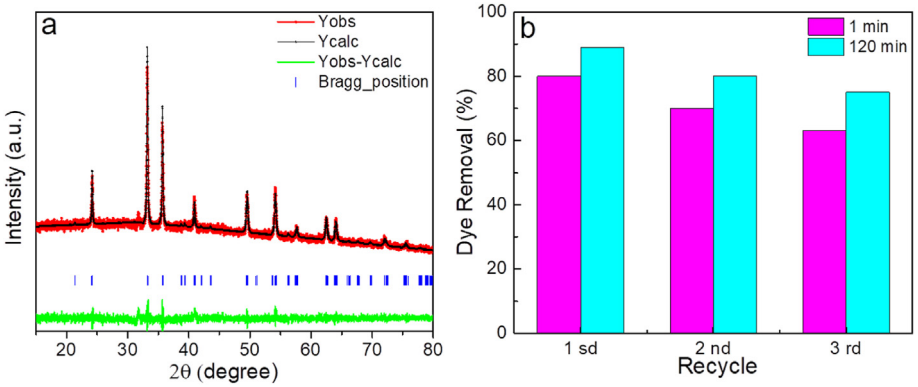

Fig. 10. (a) XRD pattern and (b) recycling tests of α-Fe_2O_3@MoS_2QDs material after photocatalytic experiment over MB.

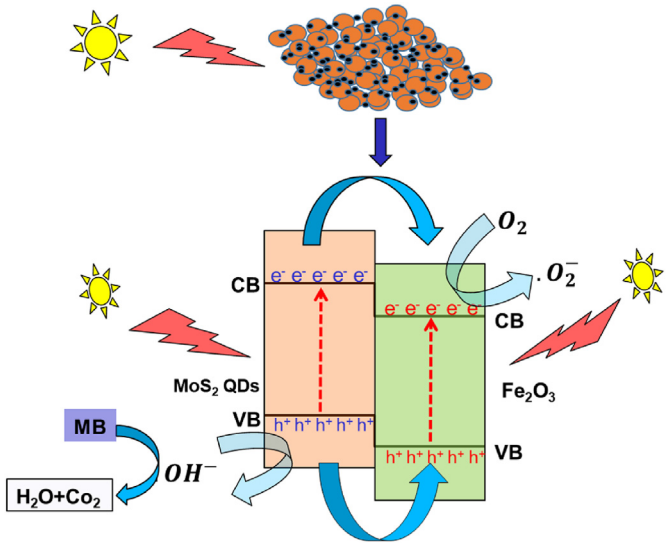

Fig. 11. Schematic description for the mechanism of photoexcited charge transfer in the α-Fe_2O_3@MoS_2QDs photocatalyst.

Besides, the low efficiency of α-Fe_2O_3 can be arising from the low hydroxyl radicals produced during the reaction. By introducing the 1T-MoS_2 QDs into the α-Fe_2O_3 to form α-Fe_2O_3@MoS_2QDs heterostructures, the photodegradation activity of MB is drastically enhanced (Fig. 8b), compared to pure α-Fe_2O_3 and the degradation rate reached 83% with only the first 1 min, revealing the excellent photocatalytic activity of the α-Fe_2O_3@MoS_2QDs catalyst. Fig. 8.c depicts the absorption decay of MB for the α-Fe_2O_3 and α-Fe_2O_3@MoS_2QDs samples. It is observed that the efficiency of the α-Fe_2O_3 catalyst is 55% after 120 min, while the α-Fe_2O_3@MoS_2QDs heterostructures exhibit an efficiency of 83% after only 1 min and 91% after 120 min. These results reflect the role of the MoS_2 QDs in the photocatalytic activity of α-Fe_2O_3@MoS_2QDs heterostructures. Fig. 9.a shows the degradation of MB as a function of time. To identify the outstanding photocatalytic activity of the prepared α-Fe_2O_3@MoS_2QDs heterostructures, our results are compared with some materials similar that reported previously [15,22,45,47–49] (Table .3). As the results indicate, the α-Fe_2O_3@MoS_2QDs nanocomposites are the most robust photocatalyst for dyes removal compared with the published photocatalytic nanomaterials. As a significant efficiency was obtained for the first 1 min, the photodegradation experiment was done two times and the same efficiency degradation was obtained (Fig.SI1).

To better evaluate the photocatalytic performance of the prepared materials, the first and second-order kinetic models were proposed to investigate kinetics reactions of the photocatalytic degradation of MB as follow:

$$\ln(C_t/C_o) = -Kt$$

where C_o and C_t and K are the initial concentration of dye, and at time t (min) and K is the rate constant (min^{-1}), respectively. The rate constant of reaction can be obtained from the slope of the $\ln C/C_0 - Time$ relation (Fig. 9b). As shown in Fig. 8c, the rate constants of α-Fe_2O_3 is 0.00642 in 120 min, while for α-Fe_2O_3@MoS_2QDs catalyst the degradation rate is very high (0.892 K^{-1}) in the first 1 min and then decrease to 0.0049 K^{-1} . These results indicate that the rate constant of Fe_2O_3@MoS_2QDs samples is 28 times of α-Fe_2O_3, which also suggests the superior photocatalytic efficiency of the α-Fe_2O_3@MoS_2QDs.

The enhanced photocatalytic efficiency of α-Fe_2O_3 after loading MoS_2 QDs is primarily attributable to the following reasons; in the α-Fe_2O_3@MoS_2QDs heterostructures, the small size of MoS_2 QDs dots well attached to the Fe_2O_3 surface enables the movement of an electron from Fe_2O_3 to MoS_2 QDs in a small distance. Additionally, the high electrical conductivity of MoS_2 QDs can quickly transfer an electron to the surface. Moreover, the considerable improvement in the visible light absorption ability and the notable decrease of the bandgap of the α-Fe_2O_3@MoS_2QDs heterostructures, which can be ascribed to the formation of multiple interfacial states at the heterojunction between α-Fe_2O_3 and MoS_2QDs, results in a considerable enhancement in the photogenerated carriers' separation and therefore high photocatalytic activity. Also, the high abundant active sites of MoS_2 QDs and network created with α-Fe_2O_3 quicken the transport of the photo-excited electrons. The ultrasmall size of MoS_2 QDs can act as electron reservoirs and, at the same time, can provide effective reaction sites for dyes degradation. Fig. 10a shows the XRD of α-Fe_2O_3@MoS_2QDs material after the reaction toward MB. It can be seen that the crystal structure is similar to that before the reaction, and no peaks were observed for MB. The recycling experiments were performed by repeating the photocatalytic process for 3 cycles as shown in Fig. 10b. The results indicate that the α-Fe_2O_3@MoS_2QDs photocatalyst exhibit good degradation efficiency in the three successive cycles. These results revealed that the α-Fe_2O_3@MoS_2QDs has good photostability stability for removing MB from water during the photocatalytic experiment.

Based on the analysis above, we can infer that the loading of MoS_2 QDs on the α-Fe_2O_3 surface can strongly enhance the photocatalytic efficiency of the α-Fe_2O_3. A schematic description of the proposed mechanism is presented in Fig. 11. Under visible light irradiation, an electron-hole pairs are generated in α-Fe_2O_3. The electrons (e−) in the valence band (VB) of α-Fe_2O_3 and MoS_2 QDs are excited to the conduction band (CB), leaving a hole (h^+) in the valence of Fe_2O_3 and MoS_2 QDs respectively. Due to the good contact between Fe_2O_3 and MoS_2 QDs, and the CB of Fe_2O_3 is more positive than MoS_2, the photoexited electrons fastly transfer from the CB of MoS_2 QDs to the lower CB of Fe_2O_3 and then migrated immediately to the surface of the catalyst through the interfacial states. Also, the generated holes in the Fe_2O_3 valence are transferred to the MoS_2 VB. The ultrasmall size of MoS_2 QDs that are well connected to the Fe_2O_3 surface supports the electron transfer between MoS_2 QDs and the Fe_2O_3. Moreover, the good electrical conducting of MoS_2 QDs will easily and quickly help the electrons to transferee to the surface. In the meantime, a superoxide anion radical ($.O_2^-$) can be creating through trapping the electrons by absorbed O_2 [50]. While the holes in the VB can react with H_2O forming highly reactive hydroxyl radicals (.OH). The superoxide radical and hydroxyl radicals are considered the principal active species for the organic dyes degradation [51] and consequently can efficiently decompose MB into CO_2.

5. Conclusion

It is extremely important to develop excellent heterojunction to enhance the photocatalytic performance of the materials. In this work, α-Fe_2O_3@MoS_2QDs photocatalyst was prepared using two-step approaches, including hydrothermal and ultrasonication approaches. The prepared materials were thoroughly characterized by X-ray diffraction (XRD), Transmission electron microscope (TEM), TGA, X-ray fluorescence (XRF) and photoluminescence spectra (PL). Structural analysis showed the formation of a single trigonal phase of Fe_2O_3 with high crystalline nature and upon introducing the MoS_2 QDs; the phase was changed to single monoclinic. Morphological and XRF measurements indicated the formation of Fe_2O_3@MoS_2QDs nanocomposites with a good distribution of MoS_2 QDs on the Fe_2O_3 surface. The superior photocatalytic degradation of Fe_2O_3@MoS_2QDs photocatalyst for MB in 1 mint was observed. The high photocatalytic degradation of the nanocomposite material may due to the formation of heterojunctions between Fe_2O_3 and MoS_2QDs, resulting in strong light absorption and high efficiency separation of carriers as demonstrated in PL analysis. An illustration mechanism of the photocatalytic degradation for MB was proposed. The present work provides a low-cost, developed heterostructure and straightforward photocatalyst fabrication method for water treatment.

Declaration of competing interest

There is no any conflict of interest.

Acknowledgements

The authors express their appreciation to the Dean ship of Scientific Research at King Khalid University for funding this work through research groups program under grant number R.G.P.2/61/40.

Appendix A. Supplementary data

Supplementary data to this article can be found online at https://doi.org/10.1016/j.ceramint.2020.05.021.

References

[1] D. Dissanayake, M. Mantilaka, T. Palihawadana, G. Chandrakumara, R. De Silva, H. Pitawala, K.N. de Silva, G. Amaratunga, Facile and low-cost synthesis of pure hematite (α-Fe 2 O 3) nanoparticles from naturally occurring laterites and their superior adsorption capability towards acid-dyes, RSC Adv. 9 (2019) 21249–21257.
[2] C. Sun, J.S. Lee, M. Zhang, Magnetic nanoparticles in MR imaging and drug delivery, Adv. Drug Deliv. Rev. 60 (2008) 1252–1265.
[3] H.-Y. Lee, Z. Li, K. Chen, A.R. Hsu, C. Xu, J. Xie, S. Sun, X. Chen, PET/MRI dual-modality tumor imaging using arginine-glycine-aspartic (RGD)–conjugated radiolabeled iron oxide nanoparticles, J. Nucl. Med. 49 (2008) 1371–1379.
[4] R. Qiao, C. Yang, M. Gao, Superparamagnetic iron oxide nanoparticles: from preparations to in vivo MRI applications, J. Mater. Chem. 19 (2009) 6274–6293.
[5] D.L. Thorek, A.K. Chen, J. Czupryna, A. Tsourkas, Superparamagnetic iron oxide nanoparticle probes for molecular imaging, Ann. Biomed. Eng. 34 (2006) 23–38.
[6] J.W. Bulte, D.L. Kraitchman, Iron oxide MR contrast agents for molecular and cellular imaging, NMR Biomed.: An International Journal Devoted to the Development and Application of Magnetic Resonance In Vivo 17 (2004) 484–499.
[7] B. Chertok, B.A. Moffat, A.E. David, F. Yu, C. Bergemann, B.D. Ross, V.C. Yang, Iron oxide nanoparticles as a drug delivery vehicle for MRI monitored magnetic targeting of brain tumors, Biomaterials 29 (2008) 487–496.
[8] K. Kavithaa, M. Paulpandi, P.R. Padma, S. Sumathi, Induction of intrinsic apoptotic pathway and cell cycle arrest via baicalein loaded iron oxide nanoparticles as a competent nano-mediated system for triple negative breast cancer therapy, RSC Adv. 6 (2016) 64531–64543.
[9] H.-L. Xu, K.-L. Mao, Y.-P. Huang, J.-J. Yang, J. Xu, P.-P. Chen, Z.-L. Fan, S. Zou, Z.-Z. Gao, J.-Y. Yin, Glioma-targeted superparamagnetic iron oxide nanoparticles as drug-carrying vehicles for theranostic effects, Nanoscale 8 (2016) 14222–14236.
[10] A.K. Gupta, M. Gupta, Synthesis and surface engineering of iron oxide nanoparticles for biomedical applications, Biomaterials 26 (2005) 3995–4021.
[11] C. Karunakaran, S. Senthilvelan, Fe2O3-photocatalysis with sunlight and UV light: oxidation of aniline, Electrochem. Commun. 8 (2006) 95–101.
[12] M. Mishra, D.-M. Chun, α-Fe2O3 as a photocatalytic material: a review, Appl. Catal. Gen. 498 (2015) 126–141.
[13] J.B.F.d.O. Baraúna, Síntese, caracterização e atividade fotocatalítica de nanocompósitos de óxido de grafeno reduzido/Hematita, (2019).
[14] H. Zhang, M. Li, C. Zhu, Q. Tang, P. Kang, J. Cao, Preparation of magnetic α-Fe2O3/ZnFe2O4@ Ti3C2 MXene with excellent photocatalytic performance, Ceram. Int. 46 (2020) 81–88.
[15] M.B. Lejbini, P. Sangpour, Hydrothermal synthesis of α-Fe2O3-decorated MoS2 nanosheets with enhanced photocatalytic activity, Optik 177 (2019) 112–117.
[16] B. Qu, Y. Sun, L. Liu, C. Li, C. Yu, X. Zhang, Y. Chen, Ultrasmall Fe 2 O 3 nanoparticles/MoS 2 nanosheets composite as high-performance anode material for lithium ion batteries, Sci. Rep. 7 (2017) 42772.
[17] K. Deshpande, A. Mukasyan, A. Varma, Direct synthesis of iron oxide nanopowders by the combustion approach: reaction mechanism and properties, Chem. Mater. 16 (2004) 4896–4904.
[18] A. Lassoued, B. Dkhil, A. Gadri, S. Ammar, Control of the shape and size of iron oxide (α-Fe2O3) nanoparticles synthesized through the chemical precipitation method, Results in physics 7 (2017) 3007–3015.
[19] S. Zhang, F. Ren, W. Wu, J. Zhou, L. Sun, X. Xiao, C. Jiang, Size effects of Ag nanoparticles on plasmon-induced enhancement of photocatalysis of Ag-α-Fe2O3 nanocomposites, J. Colloid Interface Sci. 427 (2014) 29–34.
[20] L. Peng, T. Xie, Y. Lu, H. Fan, D. Wang, Synthesis, photoelectric properties and photocatalytic activity of the Fe 2 O 3/TiO 2 heterogeneous photocatalysts, Phys. Chem. Chem. Phys. 12 (2010) 8033–8041.
[21] L.-P. Zhu, N.-C. Bing, D.-D. Yang, Y. Yang, G.-H. Liao, L.-J. Wang, Synthesis and photocatalytic properties of core–shell structured α-Fe 2 O 3@ SnO 2 shuttle-like nanocomposites, CrystEngComm 13 (2011) 4486–4490.
[22] L. Zhang, Z. Bao, X. Yu, P. Dai, J. Zhu, M. Wu, G. Li, X. Liu, Z. Sun, C. Chen, Rational design of α-Fe2O3/reduced graphene oxide composites: rapid detection and effective removal of organic pollutants, ACS Appl. Mater. Interfaces 8 (2016) 6431–6438.
[23] B.A. Ali, A.M. Omar, A.S. Khalil, N.K. Allam, Untapped potential of polymorph MoS2: tuned cationic intercalation for high-performance symmetric supercapacitors, ACS Appl. Mater. Interfaces 11 (2019) 33955–33965.
[24] S. Das, A.M. Tama, S. Dutta, M.S. Ali, M. Basith, Facile high-yield synthesis of MoS2 nanosheets with enhanced photocatalytic performance using ultrasound driven exfoliation technique, Mater. Res. Express 6 (2019) 125079.
[25] G.P. Awasthi, S.P. Adhikari, S. Ko, H.J. Kim, C.H. Park, C.S. Kim, Facile synthesis of ZnO flowers modified graphene like MoS2 sheets for enhanced visible-light-driven photocatalytic activity and antibacterial properties, J. Alloys Compd. 682 (2016) 208–215.
[26] Q. Xiang, J. Yu, M. Jaroniec, Synergetic effect of MoS2 and graphene as cocatalysts for enhanced photocatalytic H2 production activity of TiO2 nanoparticles, J. Am. Chem. Soc. 134 (2012) 6575–6578.
[27] M.R. Saber, G. Khabiri, A.A. Maarouf, M. Ulbricht, A.S. Khalil, A comparative study on the photocatalytic degradation of organic dyes using hybridized 1T/2H, 1T/3R and 2H MoS 2 nano-sheets, RSC Adv. 8 (2018) 26364–26370.
[28] A.M. Omar, O.I. Metwalli, M.R. Saber, G. Khabiri, M.E. Ali, A. Hassen, M.M. Khalil, A.A. Maarouf, A.S. Khalil, Revealing the Role of the 1T Phase on the Adsorption of Organic Dyes on MoS_2 Nanosheets, (2019).
[29] H. Liu, T. Lv, C. Zhu, X. Su, Z. Zhu, Efficient synthesis of MoS2 nanoparticles modified TiO2 nanobelts with enhanced visible-light-driven photocatalytic activity, J. Mol. Catal. Chem. 396 (2015) 136–142.
[30] A.K. Sharma, B. Kaur, Simulation and analysis of 2D material (MoS2/MoSe2) based plasmonic sensor for measurement of organic compounds in infrared, Optik 157 (2018) 161–169.
[31] X. Tian, Y. Sun, S. Fan, M.D. Boudreau, C. Chen, C. Ge, J.-J. Yin, Photogenerated charge carriers in molybdenum disulfide quantum dots with enhanced antibacterial activity, ACS Appl. Mater. Interfaces 11 (2019) 4858–4866.
[32] W. Qiao, S. Yan, X. Song, X. Zhang, X. He, W. Zhong, Y. Du, Luminescent monolayer MoS2 quantum dots produced by multi-exfoliation based on lithium intercalation, Appl. Surf. Sci. 359 (2015) 130–136.
[33] W. Gu, Y. Yan, C. Zhang, C. Ding, Y. Xian, One-step synthesis of water-soluble MoS2 quantum dots via a hydrothermal method as a fluorescent probe for hyaluronidase detection, ACS Appl. Mater. Interfaces 8 (2016) 11272–11279.
[34] J. Sun, L. Duan, Q. Wu, W. Yao, Synthesis of MoS2 quantum dots cocatalysts and their efficient photocatalytic performance for hydrogen evolution, Chem. Eng. J. 332 (2018) 449–455.
[35] A. O'Neill, U. Khan, J.N. Coleman, Preparation of high concentration dispersions of exfoliated MoS2 with increased flake size, Chem. Mater. 24 (2012) 2414–2421.
[36] A.M. El Sayed, G. Khabiri, Spectroscopic, optical and dielectric investigation of (Mg, Cu, Ni, or Cd) acetates' influence on carboxymethyl cellulose sodium salt/polyvinylpyrrolidone polymer electrolyte films, J. Electron. Mater., 1-12..
[37] B. Han, S. Liu, N. Zhang, Y.-J. Xu, Z.-R. Tang, One-dimensional CdS@ MoS2 core-shell nanowires for boosted photocatalytic hydrogen evolution under visible light, Appl. Catal. B Environ. 202 (2017) 298–304.
[38] Y. Huang, W. Fan, B. Long, H. Li, F. Zhao, Z. Liu, Y. Tong, H. Ji, Visible light Bi2S3/Bi2O3/Bi2O2CO3 photocatalyst for effective degradation of organic pollution, Appl. Catal. B Environ. 185 (2016) 68–76.
[39] D. Li, H. Wang, H. Tang, X. Yang, Q. Liu, Remarkable enhancement in solar oxygen evolution from MoSe2/Ag3PO4 heterojunction photocatalyst via in situ constructing interfacial contact, ACS Sustain. Chem. Eng. 7 (2019) 8466–8474.
[40] Q. Liu, J. Shen, X. Yang, T. Zhang, H. Tang, 3D reduced graphene oxide aerogel-mediated Z-scheme photocatalytic system for highly efficient solar-driven water oxidation and removal of antibiotics, Appl. Catal. B Environ. 232 (2018) 562–573.
[41] A.M. Tama, S. Das, S. Dutta, M. Bhuyan, M. Islam, M. Basith, MoS 2 nanosheet incorporated α-Fe 2 O 3/ZnO nanocomposite with enhanced photocatalytic dye degradation and hydrogen production ability, RSC Adv. 9 (2019) 40357–40367.
[42] D. Garcia, G. Picasso, P. Hidalgo, H.E. Peres, R.S. Kou, J.M. Gonçalves, Sensors based on Ag-loaded hematite (α-Fe2O3) nanoparticles for methyl mercaptan detection at room temperature, Analytical chemistry research 12 (2017) 74–81.
[43] X. Yang, H. Sun, L. Zhang, L. Zhao, J. Lian, Q. Jiang, High efficient photo-Fenton catalyst of α-Fe 2 O 3/MoS 2 hierarchical nanoheterostructures: reutilization for supercapacitors, Sci. Rep. 6 (2016) 31591.
[44] S. Frindy, M. Sillanpää, Synthesis and application of novel α-Fe2O3/graphene for visible-light enhanced photocatalytic degradation of RhB, Mater. Des. 188 (2020) 108461.
[45] L. Chen, F. He, N. Zhao, R. Guo, Fabrication of 3D quasi-hierarchical Z-scheme RGO-Fe2O3-MoS2 nanoheterostructures for highly enhanced visible-light-driven photocatalytic degradation, Appl. Surf. Sci. 420 (2017) 669–680.
[46] S. Han, L. Hu, Z. Liang, S. Wageh, A.A. Al-Ghamdi, Y. Chen, X. Fang, One-step hydrothermal synthesis of 2D hexagonal nanoplates of α-Fe2O3/graphene composites with enhanced photocatalytic activity, Adv. Funct. Mater. 24 (2014) 5719–5727.
[47] W.-K. Jo, N.C.S. Selvam, Synthesis of GO supported Fe 2 O 3–TiO 2 nanocomposites for enhanced visible-light photocatalytic applications, Dalton Trans. 44 (2015) 16024–16035.
[48] P. Shao, J. Tian, B. Liu, W. Shi, S. Gao, Y. Song, M. Ling, F. Cui, Morphology-tunable ultrafine metal oxide nanostructures uniformly grown on graphene and their applications in the photo-Fenton system, Nanoscale 7 (2015) 14254–14263.
[49] S. Sun, M. Sun, Y. Kong, Y. Fang, Y. Yao, MoS 2 and graphene as dual, cocatalysts for enhanced visible light photocatalytic activity of Fe 2 O 3, J. Sol. Gel Sci. Technol. 80 (2016) 719–727.
[50] J. Li, X. Ji, X. Li, X. Hu, Y. Sun, J. Ma, G. Qiao, Preparation and photocatalytic degradation performance of Ag3PO4 with a two-step approach, Appl. Surf. Sci. 372 (2016) 30–35.
[51] S. Han, L. Hu, N. Gao, A.A. Al-Ghamdi, X. Fang, Efficient self-assembly synthesis of uniform CdS spherical nanoparticles-Au nanoparticles hybrids with enhanced photoactivity, Adv. Funct. Mater. 24 (2014) 3725–3733.